

# Nitrogen-Doped Graphene: Efficient Growth, Structure, and Electronic Properties

D. Usachov,<sup>\*,†</sup> O. Vilkov,<sup>†</sup> A. Grüneis,<sup>‡,§</sup> D. Haberer,<sup>‡</sup> A. Fedorov,<sup>†</sup> V. K. Adamchuk,<sup>†</sup> A. B. Preobrazhenski,<sup>||</sup> P. Dudin,<sup>⊥</sup> A. Barinov,<sup>⊥</sup> M. Oehzelt,<sup>||</sup> C. Laubschat,<sup>#</sup> and D. V. Vyalikh<sup>†,¶</sup>

<sup>†</sup>St. Petersburg State University, St. Petersburg, 198504, Russia

<sup>‡</sup>IFW Dresden, P.O. Box 270116, D-01171 Dresden, Germany

<sup>§</sup>Faculty of Physics, Vienna University, Strudlhofgasse 4, 1090 Wien, Austria

<sup>||</sup>MAX-lab, Lund University, Box 118, 22100 Lund, Sweden

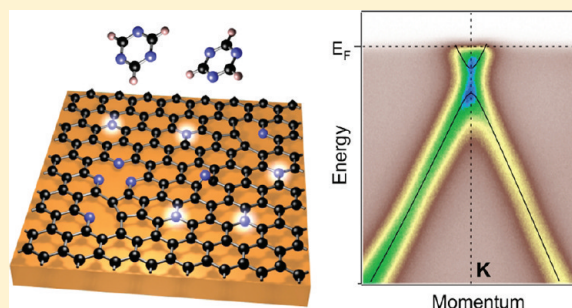
<sup>⊥</sup>Sincrotrone Trieste S.C.p.A., Area Science Park, I-34012 Basovizza, Trieste, Italy

<sup>¶</sup>Helmholtz-Zentrum Berlin für Materialien und Energie, BESSY II, Albert-Einstein-Strasse 15, D-12489 Berlin, Germany

<sup>#</sup>Institute of Solid State Physics, Dresden University of Technology, D-01062 Dresden, Germany

**ABSTRACT:** A novel strategy for efficient growth of nitrogen-doped graphene (N-graphene) on a large scale from *s*-triazine molecules is presented. The growth process has been unveiled in situ using time-dependent photoemission. It has been established that a postannealing of N-graphene after gold intercalation causes a conversion of the N environment from pyridinic to graphitic, allowing to obtain more than 80% of all embedded nitrogen in graphitic form, which is essential for the electron doping in graphene. A band gap, a doping level of 300 meV, and a charge-carrier concentration of  $\sim 8 \times 10^{12}$  electrons per  $\text{cm}^2$ , induced by 0.4 atom % of graphitic nitrogen, have been detected by angle-resolved photoemission spectroscopy, which offers great promise for implementation of this system in next generation electronic devices.

**KEYWORDS:** Graphene, nitrogen doping, electronic structure, synthesis, triazine, ARPES



Graphene is one of the amazing recent developments in modern science and one of the most promising materials for implementation in the next generation electronic devices. Because of graphene's unique properties, devices based on mechanisms alternative to classical charge transport come into reach that would allow unprecedented speed of the graphene-based transistors. However, being a zero-gap semiconductor, pure graphene does not seem to be ready for its direct implementation. Presently, many research efforts are directed toward the elaboration of methods that allow inducing and fine-tuning of a band gap in graphene.<sup>1–3</sup> We have recently demonstrated that graphene hydrogenation, that is, treatment with atomic hydrogen, gives rise to changes in the electronic properties and allows one to induce of a gap in graphene's electronic structure due to rehybridization from  $\text{sp}^2$ - to  $\text{sp}^3$ -bonded carbon upon hydrogenation, which leads to gap values of up to  $\sim 1.0$  eV at 8% hydrogen coverage.<sup>3,4</sup> The promising approach for tuning and controlling the electronic properties of graphene is doping with heteroatoms, similar to that elaborated for the silicon-based technology. Thus, doping with boron or nitrogen atoms allows graphene transformation into p- or n-type semiconductor respectively,<sup>5,6</sup> accompanied by opening of a band gap.<sup>7</sup> The ability to tune the electron–hole doping in graphene opens perspectives for developing tunable electronic devices through external control of the electron–phonon coupling.<sup>8</sup> Another

issue is that n- or p-doped graphene is also a promising candidate for applications in electrochemical biosensing,<sup>9</sup> lithium batteries,<sup>10</sup> and fuel cells.<sup>11</sup>

In the present work, we focus on the implementation of nitrogen for the n-type doping of graphene. A nitrogen atom contains one additional electron and when replacing a carbon atom in the graphene lattice, novel electronic properties can be envisaged. Generally, elaboration of recipes for incorporating nitrogen into a matrix of carbon-based materials in order to reach the desirable semiconducting properties is a rapidly developing area in the carbon technology.<sup>12–18</sup> This issue was rather intensively explored and discussed, for instance, in the scope of single-wall carbon nanotubes (CNTs),<sup>19–23</sup> which could be considered as rolled-up graphene layers. However, experimental information about the doping level and band structure of doped CNTs is still lacking. Here the study of N-graphene becomes essential, since experimentally measured band structure of N-graphene can be used to predict the band structure of N-doped CNTs by zonefolding method.<sup>24</sup>

It is widely established that incorporation of nitrogen atoms into the matrix of  $\text{sp}^2$ -bonded carbon can lead to appearance of

**Received:** September 7, 2011

**Revised:** November 9, 2011

**Published:** November 11, 2011

different kinds of nitrogen impurities. For graphene and CNTs, it was found that mainly three types of bonding may occur: (i) direct substitution (graphitic N), (ii) the pyridinic configuration, and (iii) the pyrrolic structure. Figure 1 shows a variety of possible configurations of the nitrogen impurities in graphene. Each of these configurations affects the electronic and transport properties of the functionalized material rather differently. In the graphitic configuration, three nitrogen valence electrons form three  $\sigma$ -bonds, one electron fills the  $\pi$ -states, and the fifth electron enters the  $\pi^*$ -states of conduction band, providing a strong n-doping effect.<sup>6,25</sup> However, the situation becomes more complicated for pyridinic and pyrrolic environments, and the implication of the simple tight-binding model does not predict any charge transfer effect for such impurities.<sup>25</sup> On the other hand, DFT calculations for CNTs show a lowering of the Fermi level for pyridinic and adatom configurations (p-doping), and a rising in the case of graphitic N<sup>26,27</sup> (n-doping). Graphitic N also effectively increases metallicity of CNTs.<sup>27</sup> Recent DFT calculations of N-graphene revealed p-type doping for pyridinic and pyrrolic nitrogen in graphene,<sup>28</sup> although the charge transfer per N atom is much smaller than in the case of graphitic N. Theoretical studies of the charge transport in N-graphene show that graphitic nitrogen induces n-type conductivity, preserving high mobility of charge carriers due to no defect formation upon direct substitution,<sup>6</sup> which is important for high speed electronics. Thus, graphitic nitrogen may be considered as the most efficient n-doping impurity among other bonding environments.

A few approaches have been devised recently for the synthesis of N-graphene. These are graphene electrothermal reaction with ammonia,<sup>14</sup> nitrogen plasma treatment of graphene,<sup>9,18,29</sup> chemical vapor deposition (CVD) of hydrocarbons in the presence of ammonia,<sup>11,15,30</sup> CVD with pyridine and other organic molecules,<sup>17,31</sup> CVD with liquid precursors,<sup>10</sup> and other methods.<sup>7,16,32</sup> In the present work, we discuss in detail the growth and electronic properties of quasi-freestanding N-graphene, prepared in situ by CVD from triazine molecules. This approach allows us producing single-layer graphene of high quality, thus enabling the first extensive exploration of the N-graphene band structure with photoemission (PE) and X-ray absorption techniques.

**Experimental Methods.** The studied N-graphene samples were prepared in situ by CVD of *s*-triazine ( $\text{HCN}$ )<sub>3</sub> molecules on the Ni(111) surface. For the spectroscopic experiments, we prepared Ni(111) films with a thickness of  $\sim 10$  nm grown epitaxially on the W(110) substrate in ultrahigh vacuum conditions.<sup>33</sup> The high crystalline quality of the studied samples was inferred from the sharp low energy electron diffraction (LEED) patterns observed in all cases. After preparing the Ni(111) surface, an N-graphene layer can be grown on top by CVD of ( $\text{HCN}$ )<sub>3</sub> molecules. Usually, we performed the synthesis at a vapor pressure of *s*-triazine of  $\sim 1 \times 10^{-6}$  mbar in the temperature range of 540–635 °C and exposing it for  $\sim 30$  min. The exception was a time-dependent photoemission study when the pressure was reduced to  $\sim 1.5 \times 10^{-8}$  mbar in order to slow down the reaction and for safe operation of the spectrometer. In the incipient reaction of *s*-triazine molecules with the Ni(111) surface, a graphene monolayer, containing a variety of nitrogen atom environments, is formed. Note that at these conditions the graphene growth is self-limited to one atomic layer.<sup>34–36</sup> In order to explore the electronic properties of this system we performed angle-resolved and core-level photoemission (ARPES and XPS) and X-ray absorption (NEXAFS) experiments at various

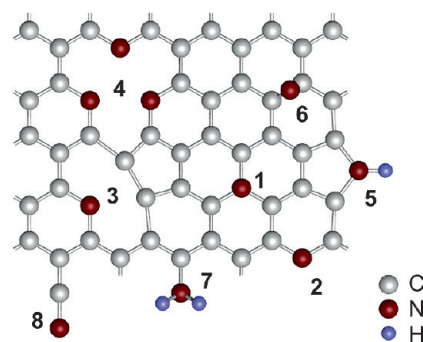


**Figure 1.** Possible configurations of nitrogen impurities in graphene: (1) substitutional or graphitic N, (2) pyridine-like N, (3) single N pyridinic vacancy, (4) triple N pyridinic vacancy, (5) pyrrole-like, (6) interstitial N or adatom, (7) amine, (8) nitrile.

facilities: (i) Elettra, at the spectromicroscopy instrument with microspot ARPES ( $\mu$ ARPES),<sup>37</sup> (ii) BESSY, at the beamline U49-2 PGM1 (time dependent XPS analysis), (iii) at the Russian-German beamline (XPS and NEXAFS) and UE52, and (iv) at the UE112-lowE-PGM beamline with a Scienta R8000 spectrometer (ARPES).  $\mu$ ARPES and ARPES measurements were performed at room temperature. To estimate the atomic concentration of nitrogen embedded into the graphene matrix, we analyzed relative intensities of the C 1s and N 1s peaks (C/N ratio). The base pressure of the experimental chamber was  $2 \times 10^{-10}$  mbar, while pressure in the *s*-triazine dosing line was  $2 \times 10^{-7}$  mbar.

**Results and Discussion.** We begin with the time-dependent photoemission experiments where the synthesis procedure is combined with the data acquisition process. Using this approach, we can follow the evolution of the N-graphene formation in real time starting from the appearance and dissociation of the first *s*-triazine molecules at the Ni(111) surface to the final construction of the N-graphene layer. For this experiment, a freshly prepared Ni(111) surface was stabilized at room temperature first. Then ( $\text{HCN}$ )<sub>3</sub> molecules were introduced into the chamber. The partial pressure of *s*-triazine was adjusted to  $\sim 1.5 \times 10^{-8}$  mbar using a leak valve. Later on, the temperature of the substrate was gradually increased from 20 to 630 °C. During the whole synthesis procedure the C 1s and N 1s electron emission signals were recorded and are depicted in Figure 2a,b, respectively.

A closer look at the evolution of the photoemission signal reveals the following details: (i) room temperature adsorption of *s*-triazine molecules leads to a manifold structure of the C 1s spectra where mainly two spectral features labeled as  $c_1$  and  $c_2$  are distinguished. The first N 1s spectra exhibit a dominant feature  $n_1$  that is accompanied by a shoulder at higher binding energy (BE). This demonstrates that the *s*-triazine molecules attach in various ways to the Ni(111) substrate. (ii) Upon increasing the temperature gradually to  $\sim 250$  °C, both C 1s and N 1s photoemission signals exhibit noticeable changes. The intensity of  $c_1$  and  $c_2$  features is decreased and their energy position is shifted to higher BE. This is accompanied by the appearance of a distinct peak at  $\sim 283.5$  eV. The shoulder  $n_2$  at  $\sim 397.3$  eV is now turned into a well-defined peak, while the intensity of the  $n_1$  feature is reduced and subsequently disappears from the N 1s spectra. This clearly indicates a dissociation of the *s*-triazine molecules on the hot Ni(111) substrate and an appearance of atomic C and N and different molecular fragments. A detailed exploration of this stage will be the subject of forthcoming studies, similar to that performed for the graphene on Ir(111) system.<sup>38</sup> (iii) Upon

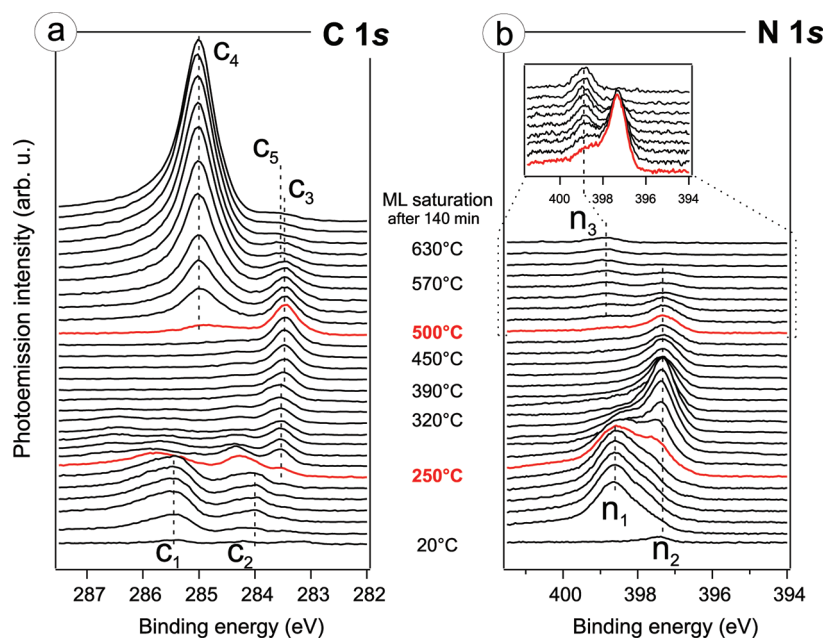


**Figure 2.** Time evolution of the photoemission intensity from the C 1s (a) and N 1s (b) core levels during the thermally stimulated dissociation of *s*-triazine molecules on the nickel substrate.

reaching a temperature of  $\sim 500^\circ\text{C}$ , the graphene related peak  $c_4$  at  $\sim 285.0$  eV starts growing. It is interesting that the evolution of the N 1s signal reveals similar behavior, as reflected by the appearance of a new spectral feature labeled  $n_3$  at  $\sim 399$  eV of BE. Note that the intensities of both peaks  $c_4$  and  $n_3$  are enhanced simultaneously. This implies that nitrogen atoms are incorporated into the graphene matrix. Gradually, the intensities of  $c_4$  and  $n_3$  features are saturated, evidencing the completion of the graphene layer, which contains a certain amount of nitrogen impurities.

Apparently, there is a certain similarity between the process described above and the synthesis of graphene from hydrocarbon substances.<sup>34</sup> However, there are also differences related to the additional presence of nitrogen that we can formulate as follows: (i) the formation of an N-graphene layer takes significantly more time, and (ii) N-graphene starts growing at essentially higher temperatures. These issues will be discussed in detail in future publication.

The particular aim of this study is to identify chemical environments associated with the incorporation of nitrogen atoms into the  $sp^2$  hybridized carbon layer, initiated by thermal dissociation of *s*-triazine molecule. To this end, N-graphene synthesized on the Ni(111) surface at a temperature of  $635^\circ\text{C}$  was liberated from the tight chemical interaction with the substrate. This was done by intercalation of gold atoms into the interface between N-graphene and Ni(111), which is a well-established procedure to bring graphene into a quasi-free-standing state.<sup>33,39,40</sup> Moreover, we anticipated that gold intercalation would help us to distinguish nitrogen atoms embedded directly into the graphene from those located at the remaining fragments of the *s*-triazine molecules or directly attached to the metallic substrate.

In Figure 3a–c, we show the evolution of the N 1s and C 1s XPS spectra, starting from a freshly prepared N-graphene layer on Ni(111), through intercalation by gold and finally, treated by postannealing. It is clear that upon gold intercalation the initial C 1s peak for N-graphene on Ni(111) exhibits a shift by  $\sim 0.6$  eV to lower BE (Figure 3c). This behavior is well-known

and associated with the breaking of strong covalent bonding between the graphene layer and the nickel surface. The obtained value is similar to that for the native (undoped) graphene on Ni(111) intercalated by gold.<sup>3</sup> This finding implies that the interaction of the native and N-graphene with the Ni(111) surface is similar.

Apparently, the samples contain nitrogen atoms in different chemical environments, as evidenced by the complex, multi-component profiles of the N 1s core-level spectra taken from the N-graphene samples (Figure 3a). The line shape of the spectra is well reproduced in a least-squares fit analysis allowing the discrimination of contributions from nitrogen atoms differently attached to graphene. Figure 3b shows the results of a deconvolution of the spectra into individual subcomponents labeled as  $N_1$ ,  $N_{2a}$ ,  $N_{2b}$ , and  $N_3$  after the signal of inelastically scattered electrons was eliminated for simplicity. The N 1s spectrum of the N-graphene/Ni(111) system is well-described by an asymmetric feature at  $\sim 399$  eV binding energy that is decomposed into the  $N_{2a}$ ,  $N_{2b}$  subcomponents. Additionally, two other peaks  $N_1$  and  $N_3$  are found at  $\sim 397.2$  and  $\sim 400$  eV BE, respectively. Upon gold intercalation, the peaks  $N_{2a}$  and  $N_{2b}$  shift to lower BE of  $\sim 398.4$  eV. The value of the shift is very close to the corresponding shift of the C 1s line. This suggests that the vast majority of nitrogen atoms, which are associated with the  $N_{2a}$  and  $N_{2b}$  lines, are embedded in the graphene layer. It is assumed that the initial asymmetry of the main feature that motivates decomposing it into the  $N_{2a}$ ,  $N_{2b}$  subcomponents is due to the different location and chemical interaction of the particular nitrogen atoms with respect to the nickel ones. Obviously, when the intercalation process is completed, the interaction with nickel is reduced, which caused  $N_2$  to become symmetric. Referring to previous publications that deal with photoemission analysis of carbon–nitrogen containing materials<sup>41,42</sup> as well as with N-graphene layers produced with other recipes,<sup>9–11,15,18,23,29,30</sup> we can conclude that the authors commonly assigned feature  $N_2$  to the pyridinic form of nitrogen that falls into the  $\sim 398.2 - 399.3$  eV BE region.



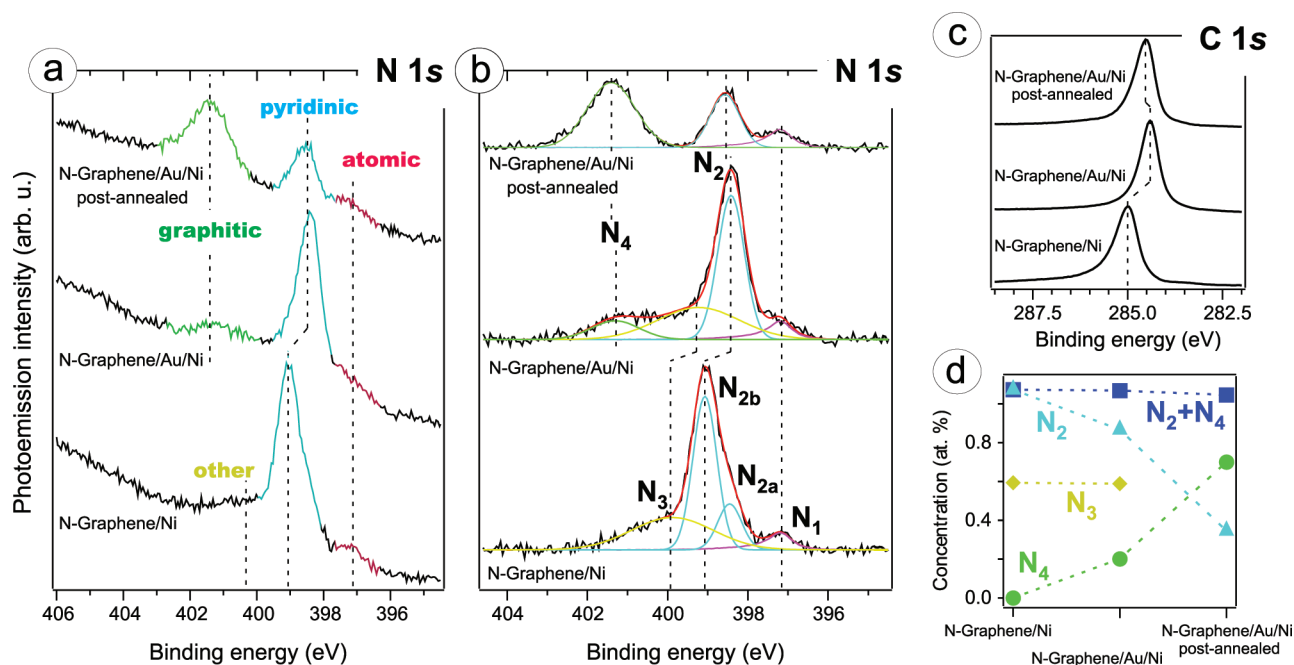


**Figure 3.** (a–c) N 1s and C 1s PE spectra of the N-graphene freshly prepared on nickel, intercalated by gold, and treated by postannealing. Background subtracted N 1s PE spectra presented in (b). (d) Atomic concentrations of the different nitrogen impurities evaluated from core-level spectra.

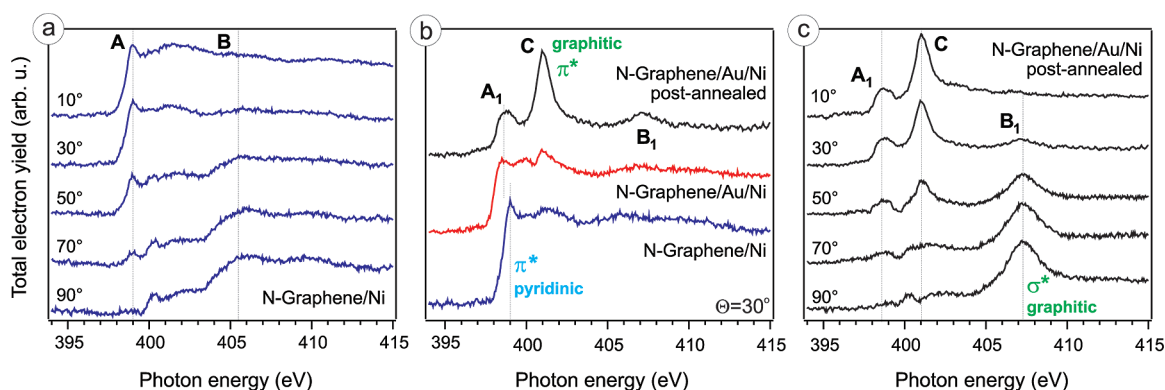


**Figure 4.** Nitrogen K-edge NEXAFS spectra taken (a) as a function of  $\theta$ , the angle between polarization vector of photons and surface normal, for N-graphene on Ni(111); (b) at  $\theta = 30^\circ$  for “as prepared” N-graphene on nickel, intercalated by gold, and treated by postannealing; (c) as a function of  $\theta$  for quasi-freestanding N-graphene after postannealing at  $\sim 500^\circ\text{C}$  for three hours.

Another interesting aspect of the gold intercalation procedure is the appearance of a new spectral feature  $N_4$ . Its BE position of  $\sim 401.3$  eV suggests that this feature is associated with nitrogen, which directly substitutes  $sp^2$  hybridized carbon, creating so-called graphitic nitrogen impurities.<sup>9–11,15,18,23,29</sup> Upon postannealing to  $\sim 500^\circ\text{C}$  the  $N_4$  intensity increases significantly, forming a well-separated peak, while the intensity of the pyridinic  $N_2$  peak is decreased. The upper spectrum in Figure 3b was taken from a sample that was annealed to  $\sim 500^\circ\text{C}$  for a few hours. Note that the major spectral modifications occur during the first hour when the growth and stabilization of the  $N_4$  peak intensity was observed. To elucidate this behavior, we summarized in Figure 3d the changes in the concentrations, corresponding to nitrogen impurities, obtained from the fit analysis of the N 1s spectra depicted in Figure 3b.

Looking at Figure 3d, the correlative behavior in the intensities of the peaks  $N_2$  and  $N_4$  can obviously be seen. Namely, the

intensity of each line is strongly affected by the intercalation and postannealing treatment while their sum remains almost unchanged. Therefore, it can be anticipated that the pyridinic nitrogen impurities are turned into the desired graphitic ones mainly by the post-annealing process. The elaboration of the transformation mechanism of the nitrogen impurities is beyond of the scope of the present study. However, we stress here that this process becomes significant only after the gold intercalation. For the N-graphene/Ni(111) system, the modification of the N 1s line shape upon postannealing was not as considerable as for N-graphene on gold. It should be noted that minor increasing of the C 1s BE after postannealing (Figure 3c) is consistent with rising of the  $E_F$  upon n-doping.

It is to be noted that neither the energy position nor the intensity of the peak  $N_1$  are affected by the intercalation and postannealing processes. This indicates that the corresponding nitrogen atoms are not embedded into graphene. Since the

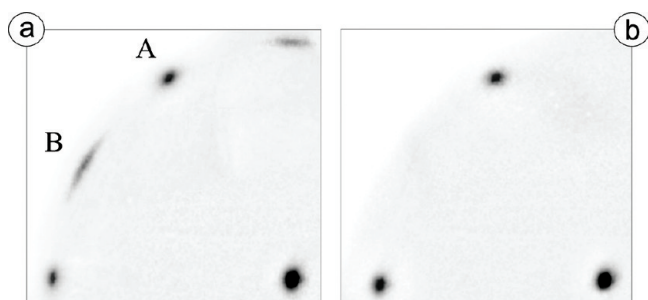


**Figure 5.** LEED patterns taken from N-graphene, synthesized at (a) 600, (b) 635 °C.

energy position of  $N_1$  peak coincides with that of  $n_2$  peak in Figure 2b, it allows us to conclude that  $N_1$  stems from the atomic nitrogen adsorbed on the nickel surface. It is not so straightforward to interpret the broad structure  $N_3$ , although its BE suggests that it can be formed by pyrrolic nitrogen content, usually found in the 400.1–400.5 eV BE region.<sup>9–11,15,18,29</sup> We can state only that after the postannealing, it does not reveal considerable contribution to the spectrum and is hard to detect after the background subtraction.

To gain further insight into the site- and symmetry- specific electronic properties of the N-graphene layer, we performed NEXAFS studies on the same set of samples. It is well-known that NEXAFS is successfully applied to explore the orientation and bond length of planar  $\pi$ -conjugated molecules adsorbed on a surface. In the recent past, it was widely used to study polarization dependence of the  $\pi$ - and  $\sigma$ -resonances for graphene- and graphite- functionalized systems. In Figure 4a–c, we show the polarization dependence of the N K-edge NEXAFS spectra taken from the freshly prepared N-graphene/Ni(111) system and after gold intercalation and postannealing, respectively. Figure 4b compares the N K-edge NEXAFS spectra from (i) native N-graphene/Ni(111), (ii) N-graphene decoupled from nickel by gold intercalation, and (iii) quasi-freestanding N-graphene after the postannealing treatment. The spectra in Figure 4a can be obviously described by two main characteristic features labeled as A and B, which are subject to polarization dependence. It can be seen that upon the gold intercalation the intensity of the peak A at  $\sim 399$  eV photon energy is reduced considerably and a second peak  $A_1$  at  $\sim 398.6$  eV occurs, which is in perfect agreement with the behavior of the  $N_2$  pyridinic feature in the N 1s core-level spectra in Figure 3. Therefore, the resonances A and  $A_1$  can be attributed to the  $N 1s \rightarrow \pi^*$  transition within the pyridinic nitrogen impurities that is also in agreement with previous NEXAFS studies of  $CN_x$ <sup>43–46</sup> and other<sup>47</sup> substances.

Upon gold intercalation a new feature C at  $\sim 401$  eV appears (Figure 4b) and its intensity increases significantly after the postannealing. Apparently, this behavior correlates well with the corresponding evolution of the  $N_4$  peak from Figure 3b. Therefore, it allows us to assign feature C to the  $N 1s \rightarrow \pi^*$  electron transition within the graphitic nitrogen environment, which is in excellent agreement with literature data.<sup>43–46</sup> The appearance of feature  $B_1$  can be associated with a  $\sigma^*$  resonance above 405 eV. Evidently, the polarization dependence of  $B_1$  and C peaks (Figure 4c) is associated with the  $\sigma^*$  and  $\pi^*$  orbitals, localized within or perpendicular to the graphitic basal planes, respectively, thus providing evidence for the existence of  $sp^2$  hybridized nitrogen incorporated into graphene.

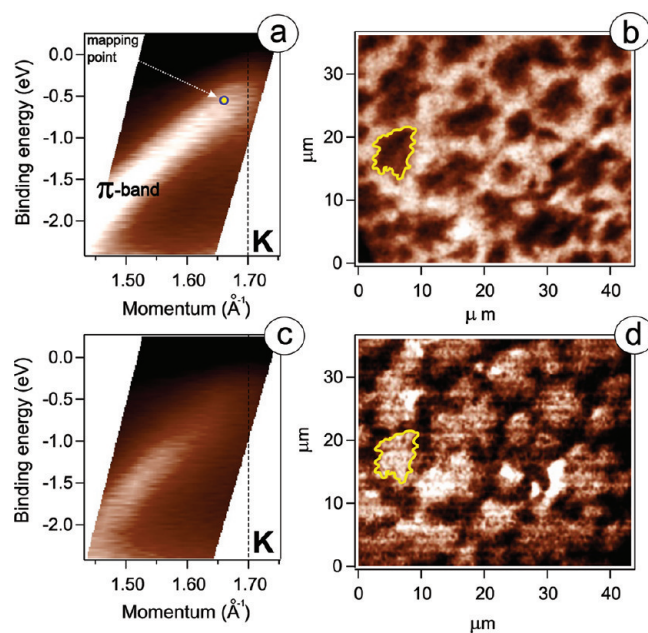


**Figure 6.** (a,c)  $\mu$ ARPES-derived photoemission spectra, acquired from the areas of A- and B-type domains of Au intercalated N-graphene with photon energy of 27 eV in the  $\Gamma K$  direction of the corresponding domains. (b,d) The real space structure of graphene domains, visualized with PE microscopy at different PE azimuthal angles, corresponding to the highest intensity of the  $\pi$ -band in the mapping point, shown in panel a. Light areas indicate high photoemission intensity.

We now discuss the morphology and the structural properties of the N-graphene layer. Figure 5a,b shows LEED patterns that we recorded from an N-graphene layer prepared at  $\sim 600$  and  $\sim 635$  °C, respectively. It can be seen that the synthesis at lower temperature leads to the appearance of a multidomain structure. The presence of at least two sorts of domains (A and B in Figure 5a) can be concluded. The A-domains exhibit a  $(1 \times 1)$  structure, just as undoped graphene/Ni(111).<sup>48</sup> The B-domains are rotated by different angles with the maximum of probability at  $30^\circ$ . However, an increase of the synthesis temperature leads to a suppression of the B-domains formation and compels the stabilization of the A-type structure. Apparently, the synthesis temperature is of decisive importance not only for the amount of various nitrogen impurities in N-graphene, but it also governs its growth properties.

To explore the microstructure of the N-graphene layer, we synthesized N-graphene at a temperature of  $\sim 600$  °C and studied it using  $\mu$ ARPES. The LEED pattern obtained from the sample was similar to that shown in Figure 5a, indicating the coexistence of two types of N-graphene domains. Exploiting anisotropy of the graphene electronic structure in the vicinity of the Fermi level, the A- and B-domains can be visualized. However, in the case of graphene/Ni the  $\pi$ -band at  $E_F$  is strongly distorted by hybridization with the Ni 3d states<sup>49</sup> and the  $\mu$ ARPES images present no visible contrast (not shown). Therefore, the  $\mu$ ARPES imaging was performed after Au intercalation, which restored the Dirac cone in the graphene electronic structure.<sup>3,40</sup> The  $\pi$ -band branch of intercalated graphene approaches  $E_F$  only at the K-points of the graphene Brillouin zone (BZ) (Figure 6a). Selectively collecting the fast  $\pi$ -electrons with a momentum of  $\sim 1.67 \text{ \AA}^{-1}$ , close to the K-point of the A-domain BZ, we recorded the photoemission microscopy image presented

in Figure 6b. It allowed a direct visualization of the domains structure in real space. In this image, the bright regions correspond to the intense photoemission signal delivered by the fast  $\pi$  electrons of the A-domains. The dark regions appear due to the local prevalence of B-domains, rotated by  $\sim 30^\circ$  and, therefore, not contributing to the PE intensity. In fact, some  $\pi$ -band intensity is still present in the dark regions, indicating that it still contains a fraction of A-domains, which are smaller than the instrument resolution ( $0.6\text{--}1\text{ }\mu\text{m}$ ). Performing a  $\mu$ ARPES scan across the same surface area, but after changing the analyzer acquisition azimuth by  $30^\circ$ , we obtained the image displayed in Figure 6d. Here the B-domains give main contribution to the PE intensity. A comparison of the highlighted regions in Figure 6b,d shows that both images are complementary. The band structure measured from B-domains is shown in Figure 6c. Its overall intensity is smaller than in the case of A-domains (Figure 6a) and the top of the  $\pi$ -band is blurred due to certain orientational disorder. It should be noted that the photoemission microscopy maps for the Au 5d states do not reveal any contrast at all. This once more implies that the observed domain structure originates from differently oriented N-graphene flakes.

Because of the limited angular resolution of the instrument ( $1.5^\circ$ ), the  $\mu$ ARPES-derived band map did not allow to explore in detail the K-point region that would give information about the doping effect induced by the N impurities. This issue was therefore explored using conventional ARPES with the high energy and momentum resolution. For this purpose, the N-graphene synthesis was performed at  $\sim 635^\circ\text{C}$  to ensure formation of high-quality layer with strong predominance of the A-type domains (see Figure 5). After subsequent Au intercalation the sample was annealed at a temperature of  $\sim 550^\circ\text{C}$  for two hours in order to convert pyridinic nitrogen into graphitic, providing noticeable electron doping effect. Figure 7a shows a band structure of such N-graphene, which exhibits two striking features. First, the Dirac cone is shifted by  $\sim 0.3\text{ eV}$  toward higher binding energies with respect to the  $\pi$ -band of undoped graphene/Au/Ni(111)/W(110), which has Dirac point directly at (or slightly above) the  $E_F$ .<sup>3,40,50</sup> A part of the conduction band appears below  $E_F$ , indicating n-type doping of graphene due to the charge transfer from N atoms. Second, a band gap of  $\sim 0.2\text{ eV}$  appears at the K-point, which is clearly visible in Figure 7b. Since undoped gold-intercalated graphene is probably gapless,<sup>50</sup> the gap originates most likely from N impurities, which break the symmetry of the graphene lattice.

Combining the ARPES and XPS data, the degree of charge transfer can be estimated. On the first step, the amount of charge in the conduction band of graphene was evaluated from the fit of ARPES data with the first-nearest-neighbor tight-binding (TB) model with Hamiltonian, described in ref 49. The model bands are shown with solid lines in Figure 7a. We have found perfect agreement with experimental data (at the K-point) at the following TB parameters:  $\varepsilon_{2p} = -0.412$ ,  $\Delta = 0.217$ ,  $\gamma_0 = -2.6$ . It corresponds to the charge-carrier density of  $8.3 \times 10^{12}$  electrons per  $\text{cm}^2$  and charge transfer of  $\sim 0.2\%$  of electron per carbon atom. On the other hand, our estimation of nitrogen concentration from XPS gives  $\sim 0.4\text{ atom } \%$  of graphitic nitrogen (Figure 7c). Further, we can neglect the influence of pyridinic nitrogen on the electronic structure of N-graphene due to its minor concentration and since its theoretically predicted doping effect is much weaker than in the case of graphitic nitrogen.<sup>25,28</sup> Thus, we obtain that graphitic N atoms donate in average nearly  $\sim 50\%$  of mobile electrons to the graphene conduction band,

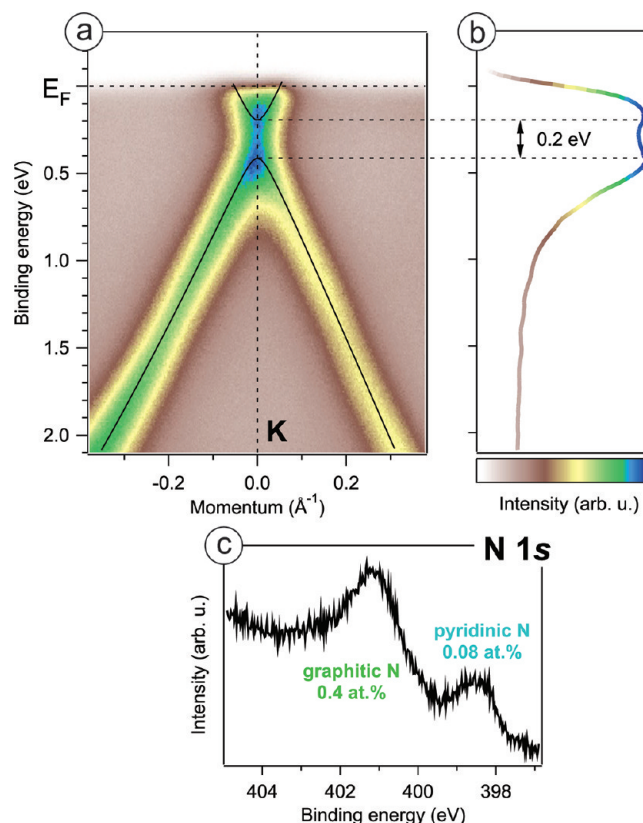


**Figure 7.** (a) ARPES of N-graphene/Au/Ni(111)/W(110), measured at the photon energy of 35 eV, through the K-point, few degrees off the direction, perpendicular to the  $\Gamma$ K. (b) PE spectrum at the K-point. (c) XPS spectrum of the same sample at N 1s core level.

which is close to the value, obtained with scanning tunneling techniques.<sup>5</sup>

In summary, a novel procedure for the nitrogen-doped graphene monolayer CVD synthesis from triazine molecules on a Ni(111) film deposited on W(110) substrate has been elaborated. A time-dependent photoemission study of the growth process has revealed that the growth mechanism is similar to the CVD of undoped graphene, however the growth rate is significantly lower due to presence of nitrogen atoms. Synthesized N-graphene layer can form domains of two types. The first domain type is formed in registry with the Ni(111) lattice, while the second is rotated by different angles close to  $30^\circ$ . The structure of domains on a micrometer scale was visualized using  $\mu$ ARPES. With increasing the synthesis temperature, the commensurate domains predominate in the layer. Obtained N-graphene is characterized by the presence of 1–2 atom % of nitrogen, which is present mainly in pyridinic form, causing minor charge transfer. However, we have developed an efficient method for converting N into graphitic form by means of Au intercalation underneath N-graphene, followed by a prolonged annealing. The study of the impact of graphitic N on the graphene band structure has revealed presence of a band gap of  $\sim 0.2\text{ eV}$ , and the  $E_F$  shift of  $\sim 300\text{ meV}$ . It also allowed direct experimental estimation of the mobile charge transferred from graphitic N to the graphene conduction band, which was found to be nearly half of electron per N atom. We anticipate that the presented approach will force further progress in utilization of N-graphene for efficient electronic applications.



## AUTHOR INFORMATION

### Corresponding Author

\*E-mail: usachov.d@googlemail.com.

## ACKNOWLEDGMENT

D.U., A.F., and V.K.A. acknowledge support through RFBR and SPbSU Grants. D.U. acknowledges support from the G-RISC program funded by the German Federal Foreign Office via the DAAD. A.G. acknowledges EU support through ELISA for the stay at BESSY, the DFG Grant GR 3708/1-1 and an APART fellowship from the Austrian Academy of Sciences. D.V. V. acknowledges the DFG Grant VY64/1-1.

## REFERENCES

- (1) Castro, E. V.; Novoselov, K. S.; Morozov, S. V.; Peres, N. M. R.; dos Santos, J. M. B. L.; Nilsson, J.; Guinea, F.; Geim, A. K.; Neto, A. H. C. *Phys. Rev. Lett.* **2007**, *99*, 216802.
- (2) Slawińska, J.; Zasada, I.; Klusek, Z. *Phys. Rev. B* **2010**, *81*, 155433.
- (3) Haberer, D.; Vyalikh, D. V.; Taioli, S.; Dora, B.; Farjam, M.; Fink, J.; Marchenko, D.; Pichler, T.; Ziegler, K.; Simonucci, S.; Dresselhaus, M. S.; Knapfer, M.; Büchner, B.; Grüneis, A. *Nano Lett.* **2010**, *10*, 3360–3366.
- (4) Haberer, D.; et al. *Adv. Mater.* **2011**, *23*, 4497–4503.
- (5) Zhao, L.; et al. *Science* **2011**, *333*, 999–1003.
- (6) Lherbier, A.; Blase, X.; Niquet, Y.-M.; Triozon, F.; Roche, S. *Phys. Rev. Lett.* **2008**, *101*, 036808.
- (7) Zhang, C.; Fu, L.; Liu, N.; Liu, M.; Wang, Y.; Liu, Z. *Adv. Mater.* **2011**, *23*, 1020–1024.
- (8) Attacalite, C.; Wirtz, L.; Lazzeri, M.; Mauri, F.; Rubio, A. *Nano Lett.* **2010**, *10*, 1172–1176.
- (9) Wang, Y.; Shao, Y.; Matson, D. W.; Li, J.; Lin, Y. *ACS Nano* **2010**, *4*, 1790–1798.
- (10) Reddy, A. L. M.; Srivastava, A.; Gowda, S. R.; Gullapalli, H.; Dubey, M.; Ajayan, P. M. *ACS Nano* **2010**, *4*, 6337–6342.
- (11) Qu, L.; Liu, Y.; Baek, J.-B.; Dai, L. *ACS Nano* **2010**, *4*, 1321–1326.
- (12) Ahlgren, E. H.; Kotakoski, J.; Krashennnikov, A. V. *Phys. Rev. B* **2011**, *83*, 115424.
- (13) Ayala, P.; F., L. F., Jr.; Rummeli, M. H.; Grüneis, A.; Pichler, T. *Phys. Status Solidi* **2007**, *244*, 40–51.
- (14) Wang, X.; Li, X.; Zhang, L.; Yoon, Y.; Weber, P. K.; Wang, H.; Guo, J.; Dai, H. *Science* **2009**, *324*, 768–771.
- (15) Wei, D.; Liu, Y.; Wang, Y.; Zhang, H.; Huang, L.; Yu, G. *Nano Lett.* **2009**, *9*, 1752–1758.
- (16) Sun, Z.; Yan, Z.; Yao, J.; Beitler, E.; Zhu, Y.; Tour, J. M. *Nature* **2010**, *468*, 549–552.
- (17) Jin, Z.; Yao, J.; Kittrell, C.; Tour, J. M. *ACS Nano* **2011**, *5*, 4112–4117.
- (18) Lin, Y.-C.; Lin, C.-Y.; Chiu, P.-W. *Appl. Phys. Lett.* **2010**, *96*, 133110.
- (19) Czerw, R.; Terrones, M.; Charlier, J.-C.; Blase, X.; Foley, B.; Kamalakaran, R.; Grobert, N.; Terrones, H.; Tekleab, D.; Ajayan, P. M.; Blau, W.; Rühle, M.; Carroll, D. L. *Nano Lett.* **2001**, *1*, 457–460.
- (20) Terrones, M.; Ajayan, P. M.; Banhart, F.; Blase, X.; Carroll, D. L.; Charlier, J. C.; Czerw, R.; Foley, B.; Grobert, N.; Kamalakaran, R.; Kohler-Redlich, P.; Rühle, M.; Seeger, T.; Terrones, H. *Appl. Phys. A* **2002**, *74*, 355–361.
- (21) Ayala, P.; Grüneis, A.; Kramberger, C.; Rummeli, M. H.; Solórzano, I. G.; F., L. F., Jr.; Pichler, T. *J. Chem. Phys.* **2007**, *127*, 184709.
- (22) Yang, S. H.; Shin, W. H.; Kang, J. K. *Small* **2008**, *4*, 437–441.
- (23) Cho, Y. J.; Kim, H. S.; Baik, S. Y.; Myung, Y.; Jung, C. S.; Kim, C. H.; Park, J.; Kang, H. S. *J. Phys. Chem. C* **2011**, *115*, 3737–3744.
- (24) Saito, R.; Dresselhaus, G.; Dresselhaus, M. S. *Physical properties of carbon nanotubes*; Imperial College Press: London, 1998.
- (25) Robertson, J.; Davis, C. A. *Diamond Relat. Mater.* **1995**, *4*, 441–444.
- (26) Zhao, M.; Xiao, Y.; Lewis, J. P.; Zhang, R. *J. Appl. Phys.* **2003**, *94*, 2398.
- (27) Lim, S. H.; Li, R.; Ji, W.; Lin, J. *Phys. Rev. B* **2006**, *76*, 195406.
- (28) Jalili, S.; Vaziri, R. *Mol. Phys.* **2011**, *109*, 687–694.
- (29) Shao, Y.; Zhang, S.; Engelhard, M. H.; Li, G.; Shao, G.; Wang, Y.; Liu, J.; Aksay, I. A.; Lin, Y. *J. Mater. Chem.* **2010**, *20*, 7491–7496.
- (30) Luo, Z.; Lim, S.; Tian, Z.; Shang, J.; Lai, L.; MacDonald, B.; Fu, C.; Shen, Z.; Yu, T.; Lin, J. *J. Mater. Chem.* **2011**, *21*, 8038–8044.
- (31) Imamura, G.; Saiki, K. *J. Phys. Chem. C* **2011**, *115*, 10000–10005.
- (32) Guo, B.; Liu, Q.; Chen, E.; Zhu, H.; Fang, L.; Gong, J. R. *Nano Lett.* **2010**, *10*, 4975–4980.
- (33) Usachov, D.; Adamchuk, V. K.; Haberer, D.; Grüneis, A.; Sachdev, H.; Preobrajenski, A. B.; Laubschat, C.; Vyalikh, D. V. *Phys. Rev. B* **2010**, *82*, 075415.
- (34) Grüneis, A.; Kummer, K.; Vyalikh, D. V. *New J. Phys.* **2009**, *11*, 073050.
- (35) Nagashima, A.; Tejima, N.; Oshima, C. *Phys. Rev. B* **1994**, *50*, 17487–17495.
- (36) Eizenberg, M.; Blakely, J. M. *Surf. Sci.* **1979**, *82*, 228–236.
- (37) Dudin, P.; Lacovig, P.; Fava, C.; Nicolini, E.; Bianco, A.; Cautero, G.; Barinov, A. *J. Synchrotron Radiat.* **2010**, *17*, 445–450.
- (38) Lizzit, S.; Baraldi, A. *Catal. Today* **2010**, *154*, 68–74.
- (39) Shikin, A. M.; Prudnikova, G. V.; Adamchuk, V. K.; Moresco, F.; Rieder, K.-H. *Phys. Rev. B* **2000**, *62*, 13202–13208.
- (40) Varykhalov, A.; Sánchez-Barriga, J.; Shikin, A. M.; Biswas, C.; Vescovo, E.; Rybkin, A.; Marchenko, D.; Rader, O. *Phys. Rev. Lett.* **2008**, *101*, 157601.
- (41) Gammon, W. J.; Kraft, O.; Reilly, A. C.; Holloway, B. C. *Carbon* **2003**, *41*, 1917–1923.
- (42) Pels, J. R.; Kapteijn, F.; Moulijn, J. A.; Zhu, Q.; Thomas, K. M. *Carbon* **1995**, *33*, 1641–1653.
- (43) Ripalda, J. M.; Román, E.; Daz, N.; Galán, L.; Montero, I.; Comelli, G.; Baraldi, A.; Lizzit, S.; Goldoni, A.; Paolucci, G. *Phys. Rev. B* **1999**, *60*, R3705–R3708.
- (44) Shimoyama, I.; Wu, G.; Sekiguchi, T.; Baba, Y. *Phys. Rev. B* **2000**, *62*, R6053–R6056.
- (45) Niwa, H.; Horiba, K.; Harada, Y.; Oshima, M.; Ikeda, T.; Terakura, K.; Ozaki, J.; Miyata, S. *J. Power Sources* **2009**, *187*, 93–97.
- (46) Choi, H. C.; Park, J.; Kim, B. *J. Phys. Chem. B* **2005**, *109*, 4333–4340.
- (47) Leinweber, P.; Kruse, J.; Walley, F. L.; Gillespie, A.; Eckhardt, K.-U.; Blyth, R.; Regier, T. *J. Synchrotron Radiat.* **2007**, *14*, 500–511.
- (48) Gamo, Y.; Nagashima, A.; Wakabayashi, M.; Terai, M.; Oshima, C. *Surf. Sci.* **1997**, *374*, 61–64.
- (49) Grüneis, A.; Vyalikh, D. V. *Phys. Rev. B* **2008**, *77*, 193401.
- (50) Varykhalov, A.; Scholz, M. R.; Kim, T. K.; Rader, O. *Phys. Rev. B* **2010**, *82*, 121101.